Hindawi Publishing Corporation
Journal of Nanomaterials
Volume 2015, Article ID 965061, 10 pages
http://dx.doi.org/10.1155/2015/965061

Research Article

Synthesis and Electrochemical Performance of Graphene Wrapped $Sn_xTi_{1-x}O_2$ Nanoparticles as an Anode Material for Li-Ion Batteries

Xing Xin, Xufeng Zhou, Tao Shen, and Zhaoping Liu

Ningbo Institute of Materials Technology & Engineering, Chinese Academy of Sciences, Zhejiang 315201, China

Correspondence should be addressed to Xufeng Zhou; zhouxf@nimte.ac.cn and Zhaoping Liu; liuzp@nimte.ac.cn

Received 4 December 2014; Revised 9 January 2015; Accepted 9 January 2015

Academic Editor: Jiamin Wu

Ever-growing development of Li-ion battery has urged the exploitation of new materials as electrodes. Here, $Sn_xTi_{1-x}O_2$ solid-solution nanomaterials were prepared by aqueous solution method. The morphology, structures, and electrochemical performance of $Sn_xTi_{1-x}O_2$ nanoparticles were systematically investigated. The results indicate that Ti atom can replace the Sn atom to enter the lattice of SnO_2 to form substitutional solid-solution compounds. The capacity of the solid solution decreases while the stability is improved with the increasing of the Ti content. Solid solution with x of 0.7 exhibits the optimal electrochemical performance. The $Sn_{0.7}Ti_{0.3}O_2$ was further modified by highly conductive graphene to enhance its relatively low electrical conductivity. The $Sn_{0.7}Ti_{0.3}O_2$/graphene composite exhibits much improved rate performance, indicating that the $Sn_xTi_{1-x}O_2$ solid solution can be used as a potential anode material for Li-ion batteries.

1. Introduction

SnO_2 has long been considered as a potential substitute for the conventional graphite anode in lithium ion batteries, since the theoretical capacity of SnO_2 (783 mAh g^{-1}) is much higher than that of commercial graphite anode (372 mAh g^{-1}) [1]. However, large volume change for SnO_2 occurs during the cycling process; thus it causes crumbling of the electrode and leads to destruction of the electrically conductive network. Therefore, the SnO_2 based anode materials suffer from rapid fading of capacity [2, 3]. There have been many strategies to improve the cycle stability of the SnO_2 based anode materials, including elaborate structure design and combination with conductive additives [3–7]. Unfortunately, the mitigation of the capacity fading is quite difficult because of the large volume change derived from alloying/dealloying reactions of Sn with Li, which is the fundamental electrochemical origin of the SnO_2 electrode [8, 9].

The SnO_2/metal oxide hybrid electrode materials, such as SnO_2-SiO_2, SnO_2-Fe_2O_3, and SnO_2-TiO_2 [10–13], have been reported to show improved electrochemical performance than pure SnO_2 for lithium storage because metal oxide can act as a buffering matrix to accommodate the large change in volume as well as the conductive additive to improve the electrical conductivity. Among these metal oxides, TiO_2 itself has also attracted great attention as an alternative anode material owing to its low cost, low toxicity, stable cyclability, and good safety. However, the practical application of the TiO_2 anode is challenging due to its low specific capacity and low intrinsic electrical conductivity which leads to limited rate capability [14–16]. There have been some reports on the SnO_2-TiO_2 mixed oxides as the anode material for Li-ion batteries. The studies involve a fundamental investigation of SnO_2-TiO_2 mixed oxides and aim to improve the cyclic performance by manipulating the morphology and content of TiO_2. Lin and coworkers [12] investigated the electrochemical performance of a TiO_2-supported SnO_2 nanocomposite formed of equimolar amounts of SnO_2 and TiO_2. The nanocomposite showed improved capacity and higher Coulombic efficiency. Du and coworkers [17] prepared three-dimensional SnO_2/TiO_2 composite by depositing SnO_2 nanocrystals into TiO_2 nanotube electrodes through solvothermal technique. The maximum reversible capacity of the composite could reach as high as ~300 μA h cm^{-2}. Except the SnO_2-TiO_2

mixed oxides, Uchiyama and coworkers [18] first proposed that the $Sn_xTi_{1-x}O_2$ solid solution could be used as the potential anode material for Li-ion batteries. They found that there was not major collapse of the structure in the $Sn_xTi_{1-x}O_2$ solid solution during lithium insertion. However, the lithium insertion/extraction behavior of this rutile-type solid solution remains unclear, and the electrochemical performance such as cyclic performance, rate performance, and resistance of this solid solution should be further tested and improved.

In this paper, a series of $Sn_xTi_{1-x}O_2$ ($0.3 \leq x \leq 0.9$) nanomaterials were successfully synthesized by an aqueous solution-based method. The morphology, structure, and the performance of $Sn_xTi_{1-x}O_2$ solid solutions as anode materials were examined in detail. The results proved that the electrochemical performance of $Sn_xTi_{1-x}O_2$ differed from either SnO_2 or TiO_2. In order to further improve its electrochemical performance, the solid solution with a certain x value was modified by graphene. The improved electrochemical performance indicates that $Sn_xTi_{1-x}O_2$/graphene composite can be used as a potential anode material for Li-ion battery.

2. Materials and Methods

2.1. Materials. All chemicals were of analytical grade and were purchased from Sinopharm Chemical Reagent Co., Ltd., China. Graphene oxide (GO) nanosheets were prepared by a chemical exfoliation process using natural graphite flakes of 300 mesh size according to the method we reported previously [19].

2.2. Preparation of $Sn_xTi_{1-x}O_2$ *Solid Solution.* Precursors of $Sn_xTi_{1-x}O_2$ solid solutions with different x values were obtained by dissolving tetrabutyl titanate (TBT) and $SnCl_2{\cdot}2H_2O$ with a certain molar ratio into 50 mL of ethanol solution under stirring at room temperature. The total concentration of the metal ions (TBT + $SnCl_2{\cdot}2H_2O$) was 0.1 M. The (TBT)/$SnCl_2{\cdot}2H_2O$ molar ratio in the precursor solutions was adjusted to 8 : 2, 7 : 3, 6 : 4, 5 : 5, 4 : 6, 3 : 7, and 2 : 8. After 30 min, 50 mL of deionized water was added into the solution. The resulting white slurry was stirred for another 1 h and additionally aged for 8 h. The precipitate was collected by centrifuge and repeatedly washed with ethanol and then air-dried at 80°C for 10 h. Different from the $Ti_xSn_{1-x}O_2$ reported by Uchiyama et al. under the same calcination temperature [18], the obtained sample was further calcinated at 500°C–900°C for 5 h, resulting in the final solid solutions. In order to compare, we prepared TiO_2 and SnO_2 particles with the precursor solutions only containing TBT or $SnCl_2{\cdot}2H_2O$, respectively.

2.3. Preparation of $Sn_xTi_{1-x}O_2$*/Graphene Composite.* $Sn_{0.7}Ti_{0.3}O_2$ was mixed with the GO solution to form a slurry with the weight ratio of $Sn_{0.7}Ti_{0.3}O_2$: GO = 4 : 1. The solid content of the slurry was adjusted to 10% by adding deionized water. After being ultrasonically exposed for 10 min, the slurry was spray-dried with an inlet air temperature of 200°C to form solid powders. The composite was then annealed at 500°C under Ar to form $Sn_{0.7}Ti_{0.3}O_2$/G composite.

2.4. Structural Characterization. Powder X-ray diffraction (XRD) measurements were performed using AXS D8 Advance diffractometer (Cu Kα radiation; receiving slit, 0.2 mm; scintillation counter, 40 mA; 40 kV) from Bruker Inc. The morphology and structure were analyzed by a Hitachi S-4800 field emission scanning-electron microscope (SEM) and FEI Tecnai G^2 F20 transmission-electron microscope (TEM) at an accelerating voltage of 200 kV.

2.5. Electrochemical Tests. The evaluation of electrochemical performance was carried out using CR2032-type coin cells. The working electrode contained 80 wt % of active materials, 10 wt% of Super P, and 10 wt % of polyvinylidene fluoride (PVDF). The Li metal foil served as the counter electrode. The electrolyte was composed of 1 M $LiPF_6$ solution in ethylene carbonate (EC)/dimethyl carbonate (DMC) (1 : 1 by volume). The coin cells were activated at a current density of 50 mA g^{-1} for the first cycle and then cycled under different current densities within the voltage range of 0.01–2 V using a LAND-CT2001A battery test system (Jinnuo Wuhan Corp., China). Cyclic voltammogram analysis was performed using Autolab 83710. Specific resistance of $Sn_xTi_{1-x}O_2$ electrode materials was measured by four-point resistivity test system (NAPSON CRESBOX) after coating the anode slurry on an insulating substrate.

3. Results and Discussion

The XRD patterns of $Sn_xTi_{1-x}O_2$ solid solutions with different x were collected to determine the crystal structures, as shown in Figure 1. All samples exhibit similar XRD patterns as that of pure rutile SnO_2 and no peaks of other crystal phase are detected, indicating that Ti does not present in the form of TiO_2 in the solid solution. When the x value of $Sn_xTi_{1-x}O_2$ decreases, all the peaks shift towards higher diffraction angles, demonstrating that the crystal structures remain the same whereas the lattice parameters of the solid solutions shrink gradually. It should be pointed out that the calcination temperature needs to be lowered to keep the pure solid solution structure at high Ti content. Though rutile TiO_2 and rutile SnO_2 both belong to tetragonal systems and the lattice parameters of two oxides are close, phase separation of TiO_2 along with solid solutions may occur especially at high Ti content. For example, at the calcination temperature of 650°C, TiO_2 are detectable when the Ti content is above 0.5. Consequently, lower calcination temperatures were adopted in our experiments to prevent the formation of TiO_2. Specifically, $Sn_{0.9}Ti_{0.1}O_2$, $Sn_{0.8}Ti_{0.2}O_2$, $Sn_{0.7}Ti_{0.3}O_2$, $Sn_{0.6}Ti_{0.4}O_2$, $Sn_{0.5}Ti_{0.5}O_2$, $Sn_{0.4}Ti_{0.6}O_2$, and $Sn_{0.3}Ti_{0.7}O_2$ were obtained at 900°C, 900°C, 800°C, 700°C, 600°C, 600°C, and 500°C, respectively. As a result of lower calcination temperature, the width of the peaks in the XRD pattern decreases with increasing Ti content, indicating that the particle size or the crystallinity of the solid solution decreases.

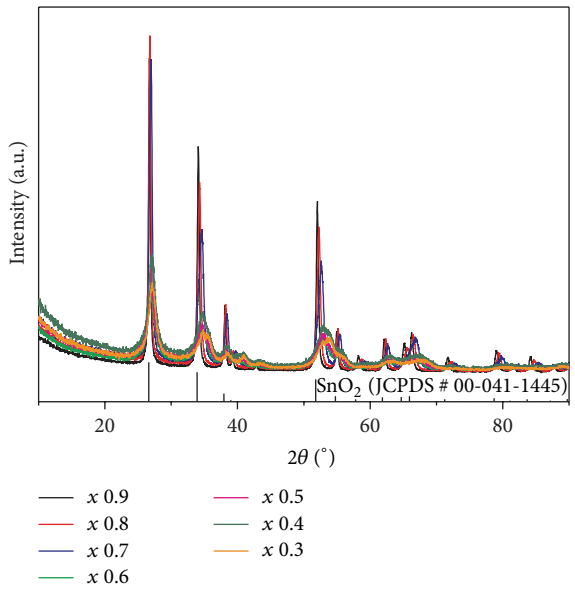

FIGURE 1: XRD patterns of $Sn_xTi_{1-x}O_2$ solid solutions with different x values.

The morphology of the precursors (before calcination) and the corresponding solid solutions were analyzed by SEM and TEM. As shown in Figures 2(a) and 2(b), both precursors of $Sn_{0.9}Ti_{0.1}O_2$ and $Sn_{0.4}Ti_{0.6}O_2$ present irregular sphere-like morphology. The particles of $Sn_{0.4}Ti_{0.6}O_2$ precursor are more significantly aggregated than that of $Sn_{0.9}Ti_{0.1}O_2$. After calcination at different temperatures, as shown in Figures 2(c) and 2(d), both $Sn_{0.9}Ti_{0.1}O_2$ and $Sn_{0.4}Ti_{0.6}O_2$ still maintain the irregular particulate morphology. The particle size of $Sn_{0.4}Ti_{0.6}O_2$ is about 10–20 nm, which is much smaller than that of $Sn_{0.9}Ti_{0.1}O_2$ (30–50 nm) (Figures 2(e) and 2(f)). The clearly visible set of lattice fringes observed in TEM images (Figures 2(g) and 2(h)) with a period of 0.334 nm and 0.328 nm is characteristic of the (101) lattice planes of rutile $Sn_xTi_{1-x}O_2$ with x of 0.9 and 0.4, respectively. The decrease of the particle size along with the increase of the Ti content is consistent with the XRD results, which is probably due to the lower calcination temperature. However, the aggregation of $Sn_xTi_{1-x}O_2$ nanoparticles becomes more severe when the Ti content increases.

X-ray photoelectron spectroscopy (XPS) analysis of the $Sn_{0.4}Ti_{0.6}O_2$ solid solution was performed in the range of 0–1200 eV, as shown in Figure 3(a). There are two symmetrical peaks at 487.15 eV and 495.60 eV in the Sn 3d spectrum (Figure 3(b)), which can be attributed to Sn $3d_{5/2}$ and Sn $3d_{3/2}$, respectively. The separation between these two peaks is 8.45 eV, slightly larger than the energy splitting reported for SnO_2 [11]. Similarly, the Ti 2p spectrum (Figure 3(c)) is also composed of two symmetrical peaks with binding energies of 459.5 eV and 465.15 eV, which are derived from Ti $2p_{3/2}$ and Ti $2p_{1/2}$, respectively. The separation of 5.65 eV between these two signals indicates a normal state of Ti^{4+} in the rutile $Sn_{0.4}Ti_{0.6}O_2$ solid solution [20]. As for the O 1s spectrum shown in Figure 3(d), the O 1s peak can be deconvoluted into two peaks at 530.70 eV and 531.95 eV, corresponding to Ti–O–Ti and Sn–O–Ti bonds, respectively [21]. It should be noted that the Ti–O–Ti bonds should be attributed to the trace of TiO_2 on the surface of solid solution especially when Ti content is high. From the Sn–O–Ti bonds it can be inferred that Ti has been successfully incorporated into the SnO_2 matrix through Sn–O–Ti bonds.

Then the solid solutions were subjected to a systematic electrochemical analysis. Cyclic voltammetry (CV) was carried out at a scan rate of 0.2 mV s^{-1} to identify the characteristics of the redox reactions during charge/discharge cycles. As can be seen from Figures 4(a), 4(b), and 4(c), all the solid solutions with different x present similar CV curves in the first cycle. The CV curves clearly indicate a reaction during the first discharge with a reduction peak around 1 V. The XRD results (Figure 4(d)) further confirm that, after the Li^+ insertion, Sn as the only crystalline phase presents in both $Sn_{0.9}Ti_{0.1}O_2$ and $Sn_{0.7}Ti_{0.3}O_2$ anode material. Therefore, the peak around 1 V is speculated to represent the reaction of Li with SnO_2 to form Li_2O and Sn, which is similar to the first discharge process of the SnO_2 based anode material as the reaction (1). For the SnO_2 based anode material, the reduction peak at 1 V disappears after the first discharge, indicating that the reaction of Li with SnO_2 to form Li_2O and Sn is generally irreversible [5, 12, 22]. After the first cycle, electrochemically reduced Sn will react with Li^+ to form a series of tin-lithium alloys during the following cycles as the reaction (2), which is reversible. On the other hand, it should be also mentioned that the insertion/extraction of Li^+ in rutile TiO_2 anode usually takes place in the potential range of 1.0–1.4 V in CV curves [23], and this process has a good reversibility as reaction (3):

$$SnO_2 + 4Li^+ + 4e^- \longrightarrow 2Li_2O + Sn \quad (1)$$

$$Sn + xLi^+ + xe^- \longleftrightarrow Li_xSn \quad (0 \le x \le 4.4) \quad (2)$$

$$TiO_2 + xLi^+ + xe^- \longleftrightarrow Li_xTiO_2 \quad (0 \le x \le 0.8) \quad (3)$$

For the $Sn_xTi_{1-x}O_2$, there is no obvious redox peak at 1.0–1.4 V in the CV curves for the solid solution, suggesting that Ti in the solid solution does not undergo a similar electrochemical reaction as that in TiO_2. Basically, the charge-discharge process of the solid solution is similar to that of SnO_2.

The initial charge-discharge curves of $Sn_{0.9}Ti_{0.1}O_2$, $Sn_{0.7}Ti_{0.3}O_2$, and $Sn_{0.4}Ti_{0.6}O_2$ solid solutions at a current density of 50 mA g^{-1} between 0.01 and 2 V are compared in Figure 5. $Sn_{0.9}Ti_{0.1}O_2$ delivers a capacity of 888 mAh g^{-1} in the first charge and 1465 mAh g^{-1} in the first discharge, while $Sn_{0.7}Ti_{0.3}O_2$ and $Sn_{0.4}Ti_{0.6}O_2$ display 780, 1225, 600, and 1125 mAh g^{-1} in the first charge and discharge, respectively. The increasing capacity of $Sn_xTi_{1-x}O_2$ with increasing x indicates that the increasing of Sn content can enhance the capacity of the solid solution. Moreover, $Sn_{0.9}Ti_{0.1}O_2$ exhibits lower irreversible capacity loss in the first cycles comparing to that of $Sn_{0.4}Ti_{0.6}O_2$. Such phenomenon may be attributed to the smaller particle size of $Sn_{0.4}Ti_{0.6}O_2$ and its lower crystallinity.

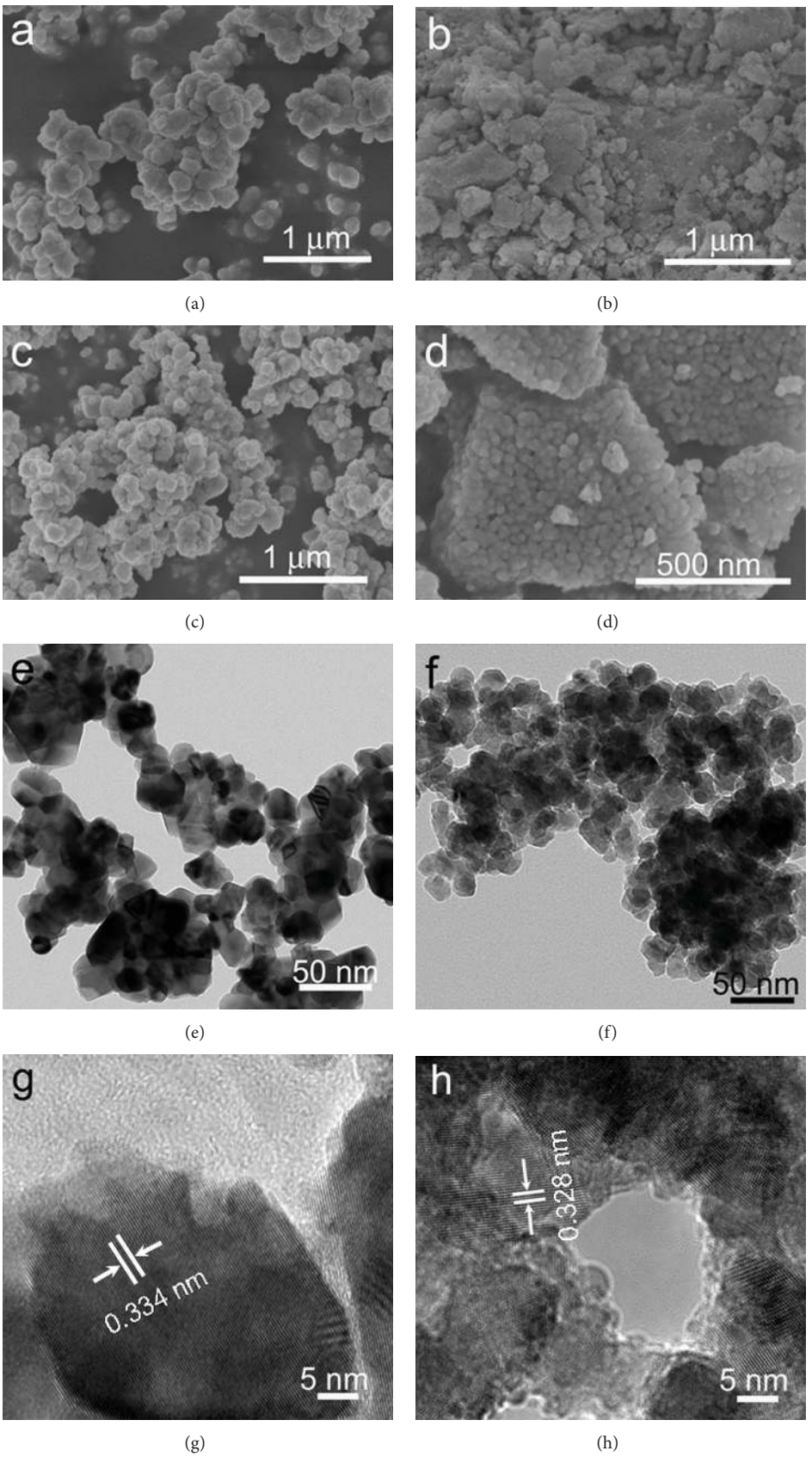

Figure 2: SEM images of the precursors of $Sn_{0.9}Ti_{0.1}O_2$ (a) and $Sn_{0.4}Ti_{0.6}O_2$ (b) solid solutions, and SEM images of $Sn_{0.9}Ti_{0.1}O_2$ (c) and $Sn_{0.4}Ti_{0.6}O_2$ (d) solid solutions. ((e), (f)) TEM images of $Sn_{0.9}Ti_{0.1}O_2$ (e) and $Sn_{0.4}Ti_{0.6}O_2$ (f) solid solutions. ((g), (h)) High-resolution TEM images of $Sn_{0.9}Ti_{0.1}O_2$ (g) and $Sn_{0.4}Ti_{0.6}O_2$ (h) solid solutions.

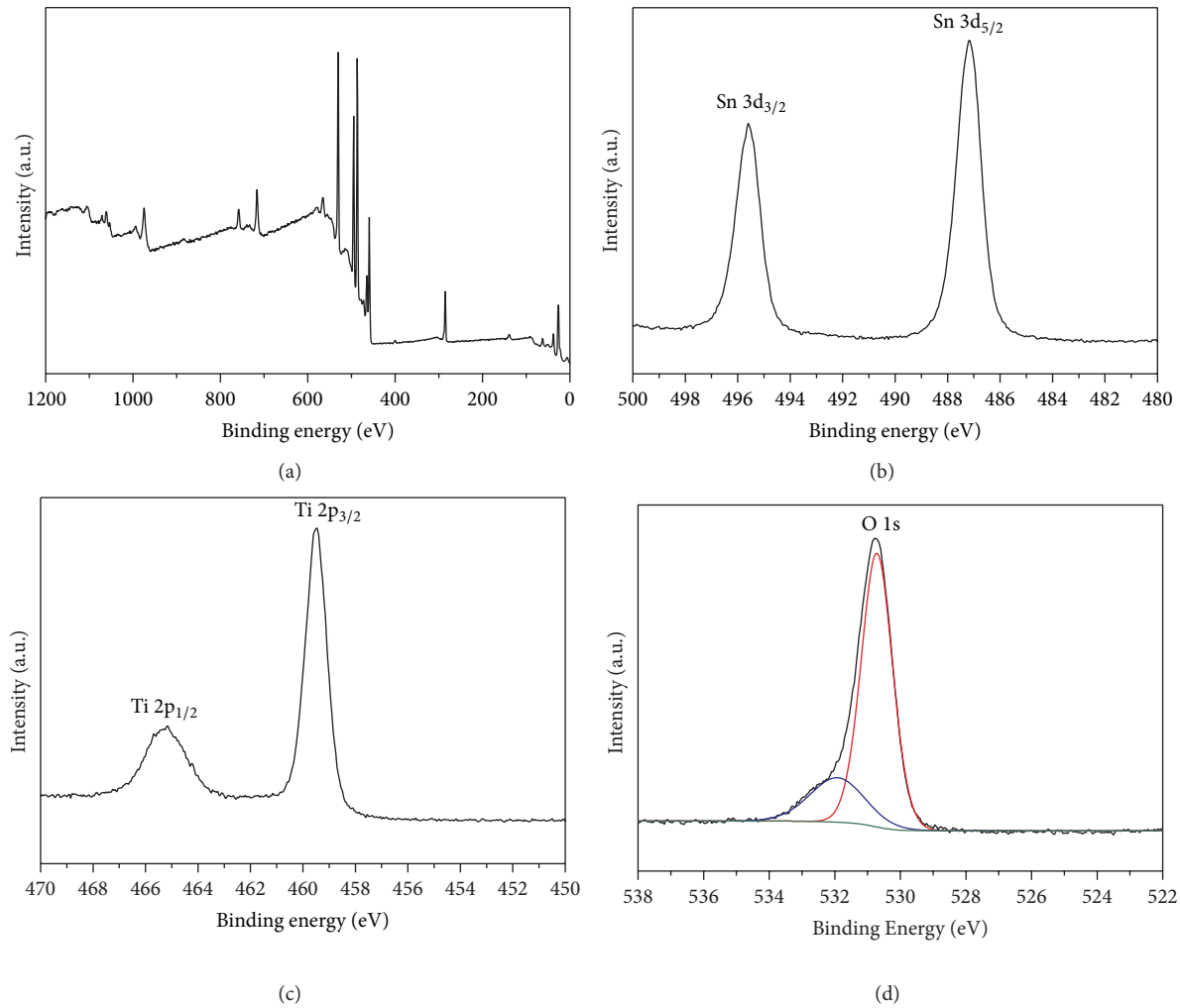

FIGURE 3: XPS spectra of the $Sn_{0.4}Ti_{0.6}O_2$ solid solutions. Panel (a) shows the survey spectrum and panels (b), (c), and (d) show the high-resolution spectra of Sn, Ti, and O, respectively.

The cycling performance of bare TiO_2, bare SnO_2, and $Sn_xTi_{1-x}O_2$ solid solution with x of 0.9, 0.7, and 0.4 was evaluated at the current density of 100 mA g^{-1}, as shown in Figure 6. The bare-TiO_2 electrode presents a stable cyclability with the reversible capacity of 200 mAh g^{-1}. The excellent cycle stability of the TiO_2 anode material should be attributed to its negligible volume change (<4%) during the charge/discharge processes. The bare-SnO_2 electrode delivers a high initial capacity of 1100 mAh g^{-1}, much higher than that of bare-TiO_2. Unfortunately, there is a rapid fading of capacity due to the severe pulverization of SnO_2 during cycling. After 30 cycles, only a low reversible capacity of 94 mAh g^{-1} is remained, which was about 10% retention of the initial reversible capacity. The $Sn_{0.9}Ti_{0.1}O_2$, $Sn_{0.7}Ti_{0.3}O_2$, and $Sn_{0.4}Ti_{0.6}O_2$ deliver the initial capacity of 887 mAh g^{-1}, 743 mAh g^{-1}, and 592 mAh g^{-1}, respectively. It is obvious that the initial capacity of $Sn_xTi_{1-x}O_2$ declines with the increasing of the Ti content but is still much higher than that of pure TiO_2. As the content of Ti increases, the cycle stability is enhanced. After 30 cycles, $Sn_{0.9}Ti_{0.1}O_2$ shows ~20% retention (174 mAh g^{-1}) of the initial capacity, which is a little higher than that of pure SnO_2 anode materials. The capacity retention can be further significantly raised to 47% and 60% when x is decreased to 0.7 ($Sn_{0.7}Ti_{0.3}O_2$) and 0.4 ($Sn_{0.4}Ti_{0.6}O_2$), respectively. With increasing Ti content, the resistivity of the solid solution also increases as displayed in Table 1. The above results thus demonstrate that the electrochemical performance of the solid solution found here is a combination of TiO_2 and SnO_2. A gradual transition of the electrochemical performance from SnO_2 to TiO_2 can be observed along with the increase of Ti content in the solid solution, and the overall electrochemical performance of $Sn_xTi_{1-x}O_2$ is strongly affected by the ratio of Ti/Sn. Consequently, with an optimal x value, the characteristic high capacity of SnO_2 anode material and superior cycle stability of TiO_2 can be optimally balanced in one solid solution anode material. Based on the above results, the optimal x value is found to be 0.7.

Despite the fact that relative good electrochemical performance can be achieved, the solid solutions still suffer

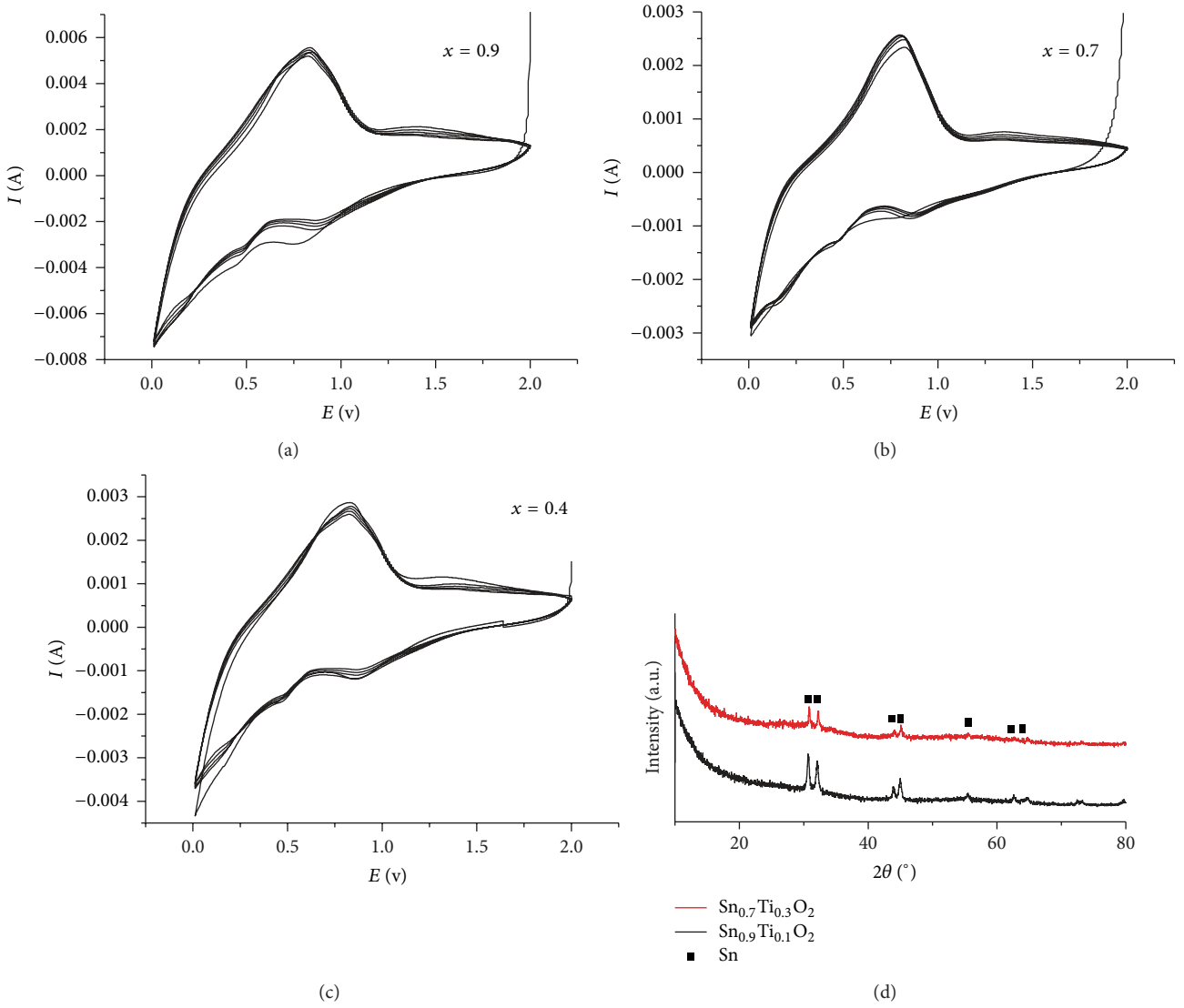

FIGURE 4: Cyclic voltammogram curves of $Sn_xTi_{1-x}O_2$ solid solution with x of 0.9 (a), 0.7 (b), and 0.4 (c) from the first cycle to the fifth cycle at a scan rate of 0.2 mV s^{-1} in the voltage range of 0.0–2.0 V. (d) XRD patterns of $Sn_{0.9}Ti_{0.1}O_2$ and $Sn_{0.7}Ti_{0.3}O_2$after Li^+ insertion.

TABLE 1: The resistance of $Sn_xTi_{1-x}O_2$ with different x tested by four probe tests.

$Sn_xTi_{1-x}O_2$	$x = 0.9$	$x = 0.8$	$x = 0.7$	$x = 0.6$	$x = 0.5$	$x = 0.4$	$x = 0.3$
R/Ω·cm	639.1	675.6	685.3	747.6	981.8	1508.3	1558.3

from low intrinsic conductivity (see Table 1). Therefore, modification of the solid solution with graphene by a spray drying method was carried out in our experiments in the case of $Sn_{0.7}Ti_{0.3}O_2$ with the optimal performance. Graphene as the 2D carbon nanomaterial was recently widely used to improve the electrochemical performance of various electrode materials due to its superior electrical conductivity, large surface area, and excellent structural flexibility [24–29]. SEM image in Figure 7(a) shows an overview of the final $Sn_{0.7}Ti_{0.3}O_2$/graphene nanocomposite. The sample consists of secondary quasispherical microparticles with diameters of 2~5 μm. SEM observation at a higher magnification (Figure 7(b)) reveals that each microsphere is actually a random aggregation of primary $Sn_{0.7}Ti_{0.3}O_2$ nanoparticles that are covered by soft graphene sheets. The TEM image further demonstrates that the $Sn_{0.7}Ti_{0.3}O_2$ nanoparticles are loosely wrapped by a thin graphene layer as presented in Figure 7(c). The high resolution TEM image (Figure 7(d)) reveals that the $Sn_{0.7}Ti_{0.3}O_2$ nanoparticles are coated with graphene shells whose thickness is less than 3 nm. In addition, the SEM and EDS mapping images show that Sn, Ti, O, and C are dispersed uniformly in the microspheres.

To further study the effects of graphene wrapping on the rate capability and cyclic stability of the solid solution,

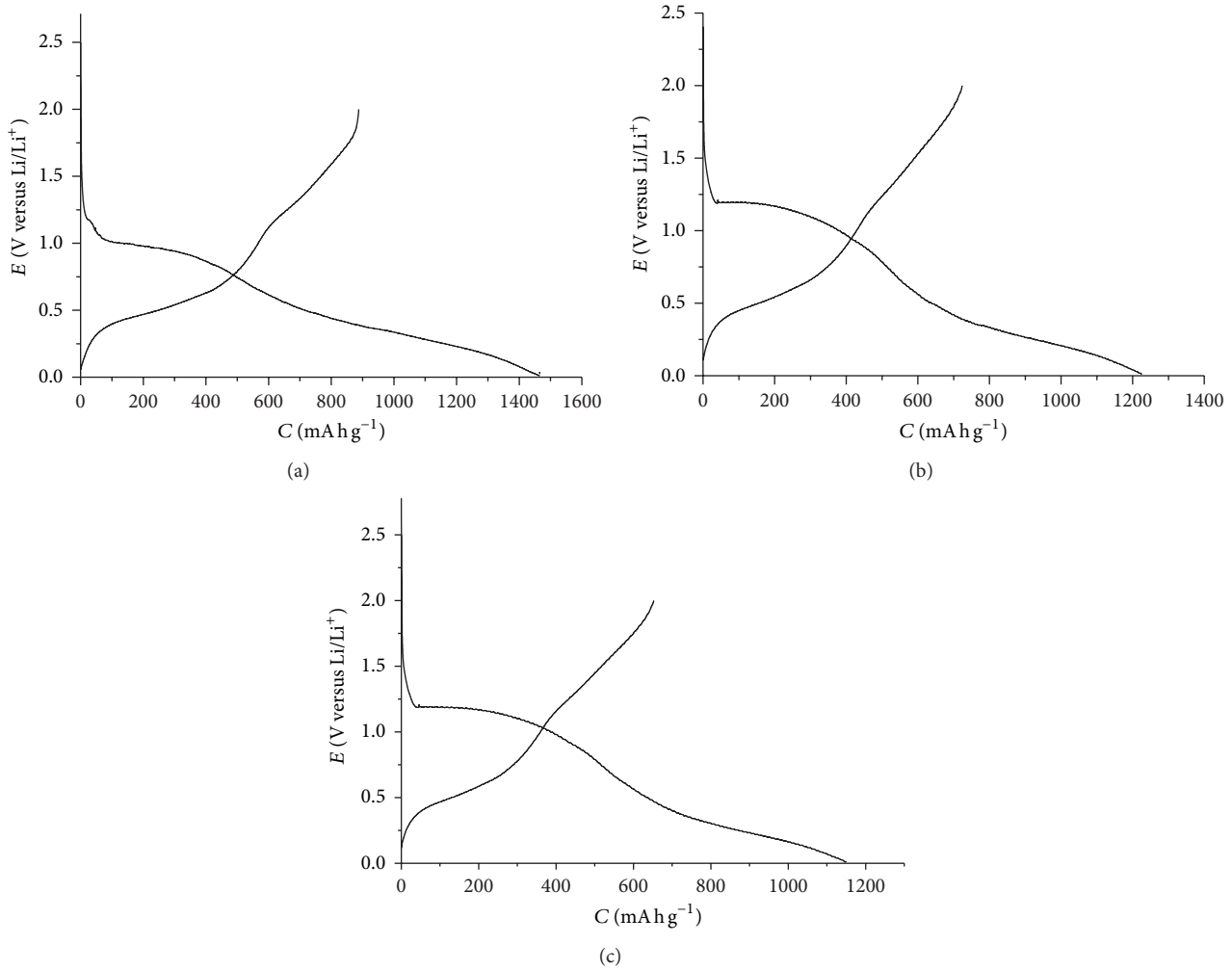

Figure 5: Initial charge-discharge curves of (a) $Sn_{0.9}Ti_{0.1}O_2$, (b) $Sn_{0.7}Ti_{0.3}O_2$, and (c) $Sn_{0.4}Ti_{0.6}O_2$ solid solutions at the current density of 50 mA g^{-1} between 0.01 and 2 V.

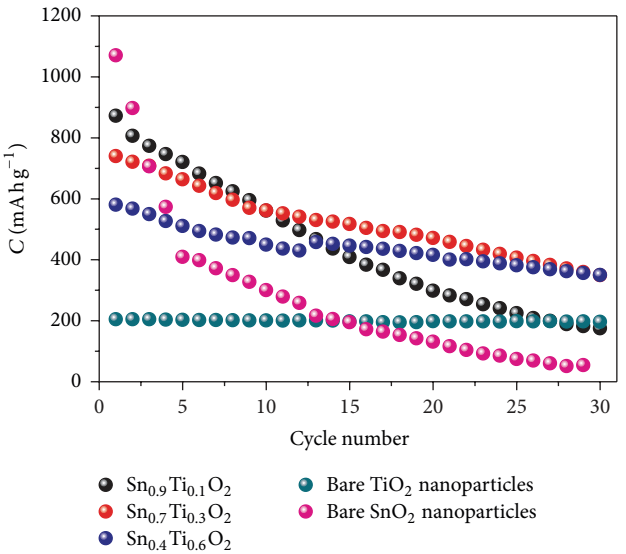

Figure 6: The capacity versus cycle number plots of $Sn_{0.9}Ti_{0.1}O_2$, $Sn_{0.7}Ti_{0.3}O_2$, and $Sn_{0.4}Ti_{0.6}O_2$ solid solutions at the current density of 100 mA g^{-1}.

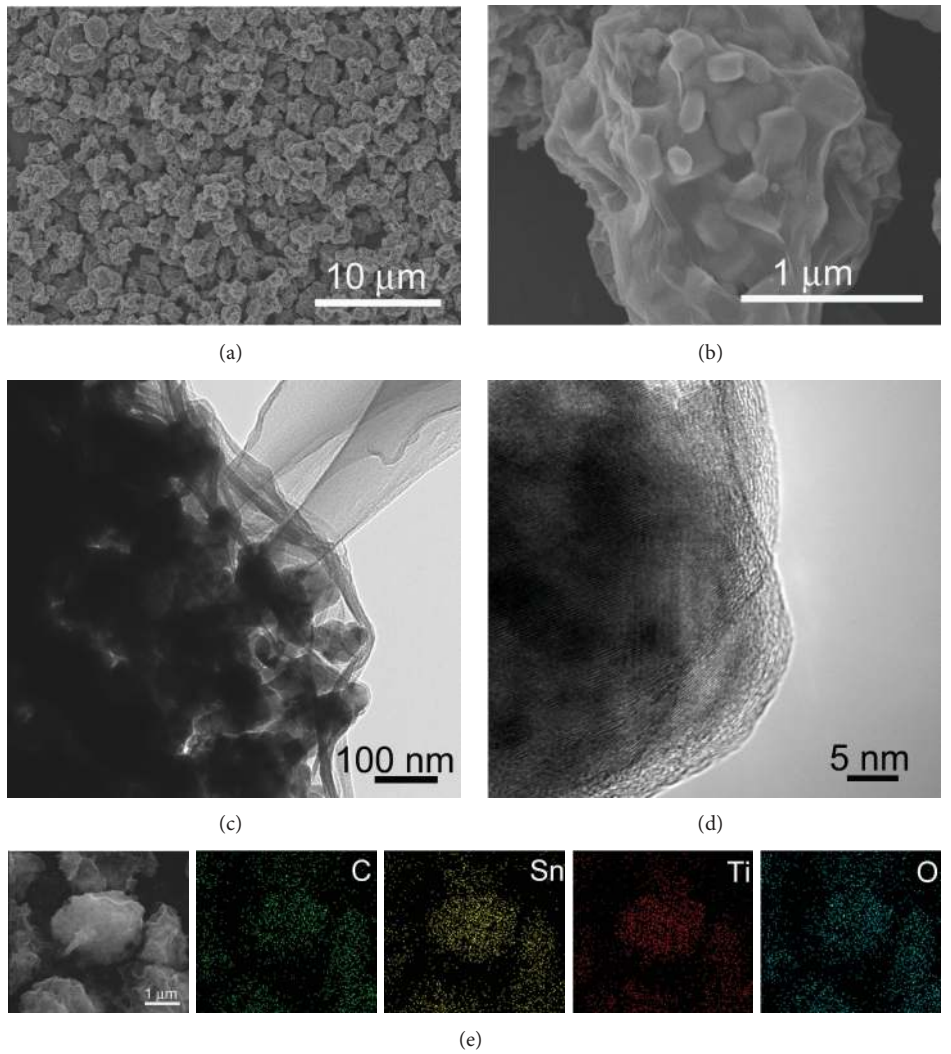

FIGURE 7: ((a), (b)) SEM images of $Sn_{0.7}Ti_{0.3}O_2$/graphene nanocomposite. (c) TEM image of $Sn_{0.7}Ti_{0.3}O_2$/graphene nanocomposite. (d) High-resolution TEM image of $Sn_{0.7}Ti_{0.3}O_2$/graphene nanocomposite. (e) SEM image and corresponding elemental map of $Sn_{0.7}Ti_{0.3}O_2$/graphene nanocomposite with green for C, red for Ti, yellow for Sn, and blue for O.

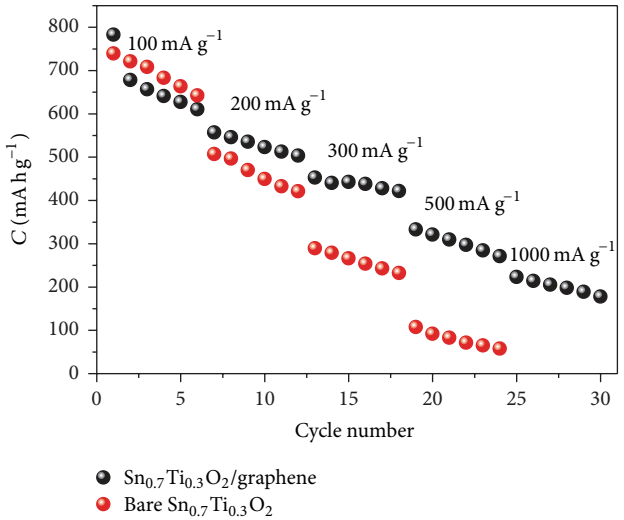

FIGURE 8: Rate capability of $Sn_{0.7}Ti_{0.3}O_2$/graphene nanocomposite and pure $Sn_{0.7}Ti_{0.3}O_2$. The charge and discharge rate was varied in the range from 100 mA g^{-1} to 1000 mA g^{-1}.

the reversible capacity of $Sn_{0.7}Ti_{0.3}O_2$/graphene nanocomposite and pure $Sn_{0.7}Ti_{0.3}O_2$ were tested with variable current densities, as plotted in Figure 8. The reversible capacity of $Sn_{0.7}Ti_{0.3}O_2$/graphene maintains 600 mAh g^{-1} at a charge rate of 100 mA g^{-1}. Further increasing the charge rates to 200 mA g^{-1}, 300 mA g^{-1}, and 500 mA g^{-1}, reversible capacities of 550 mAh g^{-1}, 470 mAh g^{-1}, and 330 mAh g can be obtained, respectively. Even at a high current density of 1000 mA g^{-1}, graphene modified solid solution can still deliver a reversible capacity of ~200 mAh g^{-1}. In contrast to $Sn_{0.7}Ti_{0.3}O_2$/graphene, $Sn_{0.7}Ti_{0.3}O_2$ electrode shows much poorer rate-performance. At the initial six cycles under the current density of 100 mA g^{-1}, the charge capacity of $Sn_{0.7}Ti_{0.3}O_2$ is slightly higher than that of $Sn_{0.7}Ti_{0.3}O_2$/graphene. However, as the current density increases, the capacity loss of the $Sn_{0.7}Ti_{0.3}O_2$ was much larger than that of the $Sn_{0.7}Ti_{0.3}O_2$/graphene. $Sn_{0.7}Ti_{0.3}O_2$ only delivers a capacity less than 100 mAh g^{-1} at a current density of 500 mA g^{-1}. The results strongly confirm that graphene conductive network can effectively improve the rate performance of the solid solution. Comparing to our previous works on the graphene modified TiO_2 and SnO_2 as anode materials for Li-ion battery, we could find that $Sn_{0.7}Ti_{0.3}O_2$/graphene presents much higher capacity than TiO_2/graphene [27, 30]. However, the cyclic life is not as high as SnO_2/graphene, which can be attributed to the large particle size of solid solution. Although more studies are required to further improve the coulombic efficiency and cyclic stability of $Sn_{0.7}Ti_{0.3}O_2$/graphene composite, we believe that it can be considered as a promising candidate for high-performance anode material in advanced LIBs.

4. Conclusion

A series of $Sn_xTi_{1-x}O_2$ solid solutions were successfully prepared by sol-gel method. The electrochemical reaction of the $Sn_xTi_{1-x}O_2$ anode material is similar to that of SnO_2. The electrochemical performance of $Sn_xTi_{1-x}O_2$ is strongly affected by the ratio of Ti/Sn, which can be regarded as a gradual transition from that of SnO_2 to TiO_2 when the x value increases. At a suitable x value of 0.7, high specific capacity and good cycle stability can be achieved simultaneously, which make $Sn_{0.7}Ti_{0.3}O_2$ a potential substitute anode material to SnO_2 or TiO_2. $Sn_{0.7}Ti_{0.3}O_2$ was further modified by graphene to enhance its electrical conductivity, which resulted in improved rate performance, indicating the potential application value of the solid solution as the anode material for Li-ion batteries.

Conflict of Interests

The authors declared that they have no conflict of interests to this work.

Acknowledgments

The authors are grateful for financial support from the Key Research Program of the Chinese Academy of Sciences (Grant no. KGZD-EW-202-4), Projects 21201173 and 21371176 supported by the National Natural Science Foundation of China, Science and Technology Innovation Team of Ningbo (Grant no. 2012B82001), and the 973 Program (Grant no. 2011CB935900).

References

[1] D. Deng and J. Y. Lee, "Hollow core-shell mesospheres of crystalline SnO_2 nanoparticle aggregates for high capacity Li^+ ion storage," *Chemistry of Materials*, vol. 20, no. 5, pp. 1841–1846, 2008.

[2] J. Fan, T. Wang, C. Yu, B. Tu, Z. Jiang, and D. Zhao, "Ordered, nanostructured tin-based oxides/carbon composite as the negative-electrode material for lithium-ion batteries," *Advanced Materials*, vol. 16, no. 16, pp. 1387–1436, 2004.

[3] Y. Wang, J. Y. Lee, and H. C. Zeng, "Polycrystalline SnO_2 nanotubes prepared via infiltration casting of nanocrystallites and their electrochemical application," *Chemistry of Materials*, vol. 17, no. 15, pp. 3899–3903, 2005.

[4] X. W. Lou, C. Yuan, and L. A. Archer, "Shell-by-shell synthesis of tin oxide hollow colloids with nanoarchitectured walls: cavity size tuning and functionalization," *Small*, vol. 3, no. 2, pp. 261–265, 2007.

[5] X. W. Lou, C. M. Li, and L. A. Archer, "Designed synthesis of coaxial SnO_2@carbon hollow nanospheres for highly reversible lithium storage," *Advanced Materials*, vol. 21, no. 24, pp. 2536–2539, 2009.

[6] H. Kim and J. Cho, "Hard templating synthesis of mesoporous and nanowire SnO_2 lithium battery anode materials," *Journal of Materials Chemistry*, vol. 18, no. 7, pp. 771–775, 2008.

[7] Z. Wen, Q. Wang, Q. Zhang, and J. Li, "In situ growth of mesoporous SnO_2 on multiwalled carbon nanotubes: a novel composite with porous-tube structure as anode for lithium batteries," *Advanced Functional Materials*, vol. 17, no. 15, pp. 2772–2778, 2007.

[8] G. Derrien, J. Hassoun, S. Panero, and B. Scrosati, "Nanostructured Sn-C composite as an advanced anode material in high-performance lithium-ion batteries," *Advanced Materials*, vol. 19, no. 17, pp. 2336–2340, 2007.

[9] M. S. Park, Y. M. Kang, J. H. Kim, G.-X. Wang, S.-X. Dou, and H.-K. Liu, "Effects of low-temperature carbon encapsulation on the electrochemical performance of SnO_2 nanopowders," *Carbon*, vol. 46, no. 1, pp. 35–40, 2008.

[10] F. Chen, Z. Shi, and M. Liu, "Preparation of mesoporous SnO_2-SiO_2 composite as electrodes for lithium batteries," *Chemical Communications*, vol. 21, pp. 2095–2096, 2000.

[11] J. Zhu, Z. Lu, M. O. Oo et al., "Synergetic approach to achieve enhanced lithium ion storage performance in ternary phased SnO_2-Fe_2O_3/rGO composite nanostructures," *Journal of Materials Chemistry*, vol. 21, no. 34, pp. 12770–12776, 2011.

[12] Y. M. Lin, R. K. Nagarale, K. C. Klavetter, A. Heller, and C. B. Mullins, "SnO_2 and TiO_2-supported-SnO_2 lithium battery anodes with improved electrochemical performance," *Journal of Materials Chemistry*, vol. 22, no. 22, pp. 11134–11139, 2012.

[13] Y.-Y. Wang, Y.-J. Hao, Q.-Y. Lai, J.-Z. Lu, Y.-D. Chen, and X.-Y. Ji, "A new composite material $Li_4Ti_5O_{12}$—SnO_2 for lithium-ion batteries," *Ionics*, vol. 14, no. 1, pp. 85–88, 2008.

[14] D. Deng, M. G. Kim, J. Y. Lee, and J. Cho, "Green energy storage materials: nanostructured TiO_2 and Sn-based anodes

for lithium-ion batteries," *Energy and Environmental Science*, vol. 2, no. 8, pp. 818–837, 2009.

[15] J. Liu, J. S. Chen, X. Wei, X. W. Lou, and X.-W. Liu, "Sandwich-like, stacked ultrathin titanate nanosheets for ultrafast lithium storage," *Advanced Materials*, vol. 23, no. 8, pp. 998–1002, 2011.

[16] I. Moriguchl, R. Hidaka, H. Yamada, T. Kudo, H. Murakami, and N. Nakashima, "A mesoporous nanocomposite of TiO_2 and carbon nanotubes as a high-rate Li-intercalation electrode material," *Advanced Materials*, vol. 18, no. 1, pp. 69–73, 2006.

[17] G. Du, Z. Guo, P. Zhang et al., "SnO_2 nanocrystals on self-organized TiO_2 nanotube array as three-dimensional electrode for lithium ion microbatteries," *Journal of Materials Chemistry*, vol. 20, no. 27, pp. 5689–5694, 2010.

[18] H. Uchiyama, E. Hosono, H. Zhou, and H. Imai, "Lithium insertion into nanometer-sized rutile-type $Ti_xSn_{1-x}O_2$ solid solutions," *Solid State Ionics*, vol. 180, no. 14–16, pp. 956–960, 2009.

[19] X. Zhou and Z. Liu, "A scalable, solution-phase processing route to graphene oxide and graphene ultralarge sheets," *Chemical Communications*, vol. 46, no. 15, pp. 2611–2613, 2010.

[20] Y. Luo, J. Luo, J. Jiang et al., "Seed-assisted synthesis of highly ordered $TiO_2\alpha$- Fe_2O_3 core/shell arrays on carbon textiles for lithium-ion battery applications," *Energy and Environmental Science*, vol. 5, no. 4, pp. 6559–6566, 2012.

[21] A. S. Sreekumaran Nair, Z. Peining, V. Jagadeesh Babu, Y. Shengyuan, P. Shengjie, and S. Ramakrishna, "Highly anisotropic titanates from electrospun TiO_2-SiO_2 composite nanofibers and rice grain-shaped nanostructures," *RSC Advances*, vol. 2, no. 3, pp. 992–998, 2012.

[22] S. Ding, D. Luan, F. Y. C. Boey, J. S. Chen, and X. W. Lou, "SnO_2 nanosheets grown on graphene sheets with enhanced lithium storage properties," *Chemical Communications*, vol. 47, no. 25, pp. 7155–7157, 2011.

[23] Y.-S. Hu, L. Kienle, Y.-G. Guo, and J. Maier, "High lithium electroactivity of nanometer-sized rutile TiO_2," *Advanced Materials*, vol. 18, no. 11, pp. 1421–1426, 2006.

[24] H. Bi, F. Huang, Y. Tang et al., "Study of $LiFePO_4$ cathode modified by graphene sheets for high-performance lithium ion batteries," *Electrochimica Acta*, vol. 88, pp. 414–420, 2013.

[25] X. Zhou, F. Wang, Y. Zhu, and Z. Liu, "Graphene modified $LiFePO_4$ cathode materials for high power lithium ion batteries," *Journal of Materials Chemistry*, vol. 21, no. 10, pp. 3353–3358, 2011.

[26] J. Yao, X. Shen, B. Wang, H. Liu, and G. Wang, "In situ chemical synthesis of SnO_2-graphene nanocomposite as anode materials for lithium-ion batteries," *Electrochemistry Communications*, vol. 11, no. 10, pp. 1849–1852, 2009.

[27] X. Wang, X. Zhou, K. Yao, J. Zhang, and Z. Liu, "A SnO_2/graphene composite as a high stability electrode for lithium ion batteries," *Carbon*, vol. 49, no. 1, pp. 133–139, 2011.

[28] P. Lian, X. Zhu, H. Xiang, Z. Li, W. Yang, and H. Wang, "Enhanced cycling performance of Fe_3O_4-graphene nanocomposite as an anode material for lithium-ion batteries," *Electrochimica Acta*, vol. 56, no. 2, pp. 834–840, 2010.

[29] W. Zhou, J. Zhu, C. Cheng et al., "A general strategy toward graphene@metal oxide core-shell nanostructures for high-performance lithium storage," *Energy and Environmental Science*, vol. 4, no. 12, pp. 4954–4961, 2011.

[30] X. Xin, X. Zhou, J. Wu, X. Yao, and Z. Liu, "Scalable synthesis of TiO_2/graphene nanostructured composite with high-rate performance for lithium ion batteries," *ACS Nano*, vol. 6, no. 12, pp. 11035–11043, 2012.